NASA/TM—2019-220305

Molecular Dynamics Simulations of Silicon Carbide, Boron Nitride and Silicon for Ceramic Matrix Composite Applications

Olanrewaju Aluko
University of Michigan-Flint, Flint, Michigan

Evan J. Pineda, Trenton M. Ricks, and Steven M. Arnold
Glenn Research Center, Cleveland, Ohio

August 2019

NASA STI Program . . . in Profile

Since its founding, NASA has been dedicated to the advancement of aeronautics and space science. The NASA Scientific and Technical Information (STI) Program plays a key part in helping NASA maintain this important role.

The NASA STI Program operates under the auspices of the Agency Chief Information Officer. It collects, organizes, provides for archiving, and disseminates NASA's STI. The NASA STI Program provides access to the NASA Technical Report Server—Registered (NTRS Reg) and NASA Technical Report Server—Public (NTRS) thus providing one of the largest collections of aeronautical and space science STI in the world. Results are published in both non-NASA channels and by NASA in the NASA STI Report Series, which includes the following report types:

- TECHNICAL PUBLICATION. Reports of completed research or a major significant phase of research that present the results of NASA programs and include extensive data or theoretical analysis. Includes compilations of significant scientific and technical data and information deemed to be of continuing reference value. NASA counter-part of peer-reviewed formal professional papers, but has less stringent limitations on manuscript length and extent of graphic presentations.

- TECHNICAL MEMORANDUM. Scientific and technical findings that are preliminary or of specialized interest, e.g., "quick-release" reports, working papers, and bibliographies that contain minimal annotation. Does not contain extensive analysis.

- CONTRACTOR REPORT. Scientific and technical findings by NASA-sponsored contractors and grantees.

- CONFERENCE PUBLICATION. Collected papers from scientific and technical conferences, symposia, seminars, or other meetings sponsored or co-sponsored by NASA.

- SPECIAL PUBLICATION. Scientific, technical, or historical information from NASA programs, projects, and missions, often concerned with subjects having substantial public interest.

- TECHNICAL TRANSLATION. English-language translations of foreign scientific and technical material pertinent to NASA's mission.

For more information about the NASA STI program, see the following:

- Access the NASA STI program home page at http://www.sti.nasa.gov

- E-mail your question to help@sti.nasa.gov

- Fax your question to the NASA STI Information Desk at 757-864-6500

- Telephone the NASA STI Information Desk at 757-864-9658

- Write to:
  NASA STI Program
  Mail Stop 148
  NASA Langley Research Center
  Hampton, VA 23681-2199

NASA/TM—2019-220305

Molecular Dynamics Simulations of Silicon Carbide, Boron Nitride and Silicon for Ceramic Matrix Composite Applications

Olanrewaju Aluko
University of Michigan-Flint, Flint, Michigan

Evan J. Pineda, Trenton M. Ricks, and Steven M. Arnold
Glenn Research Center, Cleveland, Ohio

National Aeronautics and
Space Administration

Glenn Research Center
Cleveland, Ohio 44135

August 2019

Acknowledgments

Olanrewaju Aluko thanks research engineers in the LMS department, the entire staff in the Office of Education, and the library at NASA Glenn Research Center, Cleveland, Ohio, for giving their support to undertake this research study during the summers of 2017 and 2018. The authors also thank Francisco Sola, Ram Bhatt, and Ibrahim Katampe for their support in jump starting this research work.

This work was sponsored by the
Transformative Aeronautics Concepts Program.

Level of Review: This material has been technically reviewed by technical management.

Available from

NASA STI Program
Mail Stop 148
NASA Langley Research Center
Hampton, VA 23681-2199

National Technical Information Service
5285 Port Royal Road
Springfield, VA 22161
703-605-6000

This report is available in electronic form at http://www.sti.nasa.gov/ and http://ntrs.nasa.gov/

Molecular Dynamics Simulations of Silicon Carbide, Boron Nitride and Silicon for Ceramic Matrix Composite Applications

Olanrewaju Aluko
University of Michigan-Flint
Flint, Michigan, 48502

Evan J. Pineda, Trenton M. Ricks, and Steven M. Arnold
National Aeronautics and Space Administration
Glenn Research Center
Cleveland, Ohio 44135

Abstract

A comprehensive computational molecular dynamics study is presented for crystalline α-SiC (6H, 4H, and 2H SiC), β-SiC (3C SiC), layered boron nitride, amorphous boron nitride and silicon, the constituent materials for high-temperature SiC/SiC compositions. Large-scale Atomic/Molecular Parallel Simulator software package was used. The Tersoff Potential force field was utilized to evaluate their mechanical characteristics of most of the materials, and the Reax force field was used to model silicon when the Tersoff Potential did not provide accurate results. Their mechanical behaviors were evaluated at a strain rate of 10^7/s and the results agree with the experimental data in the literature. The results are foundational for linking constituent behavior to composite performance, particularly when test data is unavailable or suspect.

Introduction

A ceramic matrix composite (CMC) can be generally described as a material system comprised of fibers or particles embedded within a ceramic matrix. For example, silicon carbide/silicon carbide (SiC/SiC) composites contain coated SiC fibers and a SiC matrix. Of particular interest for high temperature applications are SiC/SiC CMCs that utilize a fiber coating composed of boron nitride (BN) (Refs. 1 to 3).

Within a SiC/SiC CMCs, SiC can exist in several crystalline phases including α-SiC (6H, 4H, and 2H SiC), β-SiC (3C) and as an amorphous material (α-SiC) (Refs. 4 to 7). The BN coating contains amorphous BN (a-BN) with a small volume fraction of layered hexagonal BN (h-BN) (Refs. 8 and 9). Finally, some unreacted silicon (Si) from processing exists in a crystalline (c-Si) or amorphous structure (α-Si). The molecular structure of the phases within the fiber, matrix, and coating influence the thermo-mechanical behavior of the composite and can be controlled through a combination of material processing methods including chemical vapor infiltration, melt infiltration, and polymer impregnation and pyrolysis (Refs. 10 and 11).

Because of flexibility in the arrangement of the different phases within a given constituent, in addition to the morphology of the constituents (fibers and coating within the matrix) themselves, it may be possible to design SiC/SiC composites to meet specific performance requirements. Validated numerical simulations can be utilized during the material design process, effectively widening the available design space and allowing for exploration of novel microstructures at a relatively low expense and rapid throughput compared to physical material production and testing. To achieve this, accurate data for the thermo-mechanical properties of the basic phases of the constituent materials in the composite must first be obtained through experimentation or simulation.

Bosak et al. (Ref. 12) determined five independent elastic moduli of single-crystal hexagonal boron nitride (h-BN) using inelastic x-ray scattering. Their results provide solid foundation for further

theoretical advances and quantitative input to models including BN nanotubes. Kamitani et al. (Ref. 13) determined the elastic constants of 4H and 6H SiC single crystals by Brillouin scattering. Harris (Ref. 14) determined the elastic moduli of β-SiC. Pozzi et al. (Ref. 15) determined the mechanical properties of a 3C-SiC film using cantilevers and bridges in SiC. Zhi et al. (Ref. 16) fabricated ultrathin boron nitride nanosheets, and detailed morphological and structural microscopic studies were performed. They found that polymeric composites containing BN nanosheets exhibited a significant reduction of the coefficient of thermal expansion (CTE) and possessed enhanced elastic modulus and strength. Jackson et al. (Ref. 17) measured the elastic modulus, strength, and Poisson's ratio of two different silicon carbides and detailed the techniques utilized to obtain these results.

Li et al. (Ref. 18) studied the effect of amorphous carbon coatings on the mechanical behavior of SiC nanowires via molecular dynamics methods at room temperature. Their results showed that amorphous carbon coatings can shield opening cracks in nanowires, making them damage-tolerant. Crocombette et al. (Ref. 19) performed nonequilibrium molecular dynamics (MD) modeling to determine the thermal conductivity of irradiated SiC as a function of cascade overlap using a Tersoff type empirical potential. Their calculated dependence of conductivity on irradiation dose was consistent with the experimental measurements of conductivity at low temperature irradiation. Zhao and Xue (Ref. 20) performed MD simulations to investigate the mechanical properties of hybrid graphene and h-BN sheet with the concentration of BN ranging from 0 to 100 percent. They showed that the Young's modulus of the hybrid sheet decreased with increasing concentration of BN, irrespective of BN shapes and distributions. Natsuki et al. (Ref. 21) predicted the elastic properties of BN nanosheets using a molecular mechanics model and the simulated result shows that BN nanosheets exhibit an isotropic elastic material behavior. Some authors (Refs. 22 to 26) also investigated the mechanical and electronic properties of h-BN nanosheets using density functional theory (DFT) calculations and achieved good agreement with existing experimental data available in the open literature.

The focus of the current work is to develop foundational atomic scale models for the different phases, SiC, BN, and Si, that appear within a SiC/SiC CMC. This is preliminary work towards establishing a multiscale modeling framework to enable a link between the molecular structure of the materials phases, the arrangement of the phases in the constituents, and the morphology of the constituents in the composite to the performance of the composite material. Measuring the properties at such a small length scale is challenging and costly. Moreover, experimental data at this scale may contain some unquantified error, and computational modeling can be used to verify experimental results and conclusions. Thus, the first step in the advancement of the multiscale framework is to establish and validate MD simulations to predict the mechanical properties of the different possible material phases in a SiC/SiC composite. In this study, MD models of α-SiC (6H, 4H, and 2H SiC), β-SiC (3C), amorphous BN (a-BN), h-BN, and crystalline Si were generated using Large-scale Atomic/Molecular Massively Parallel Simulator (LAMMPS) in order to predict their elastic properties. Data from these models were compared to experimental results, where available. Furthermore, three realizations for each material system were independently developed and evaluated to compute average properties in order to remove some level of uncertainty related to the stochastic nature of the simulated data.

The Modeling of Micro Constituents

Modeling and Simulation of Crystalline SiC and Layered BN

The crystalline SiC polytypes (α and β structures) and h-BN were constructed, as shown in Figure 1 to Figure 5, using the LAMMPS package with Tersoff potentials. This potential is chosen because it is computationally efficient. At first, the primitive cells with periodic boundary conditions for all structures were constructed. Then, the supercell crystalline model of each structure was created by replicating the primitive cell in the X-, Y-, and Z-directions. Specifically, the α-SiC (6H-, 4H-, and 2H-SiC) structure was modeled using the primitive vectors given by Reference 17.

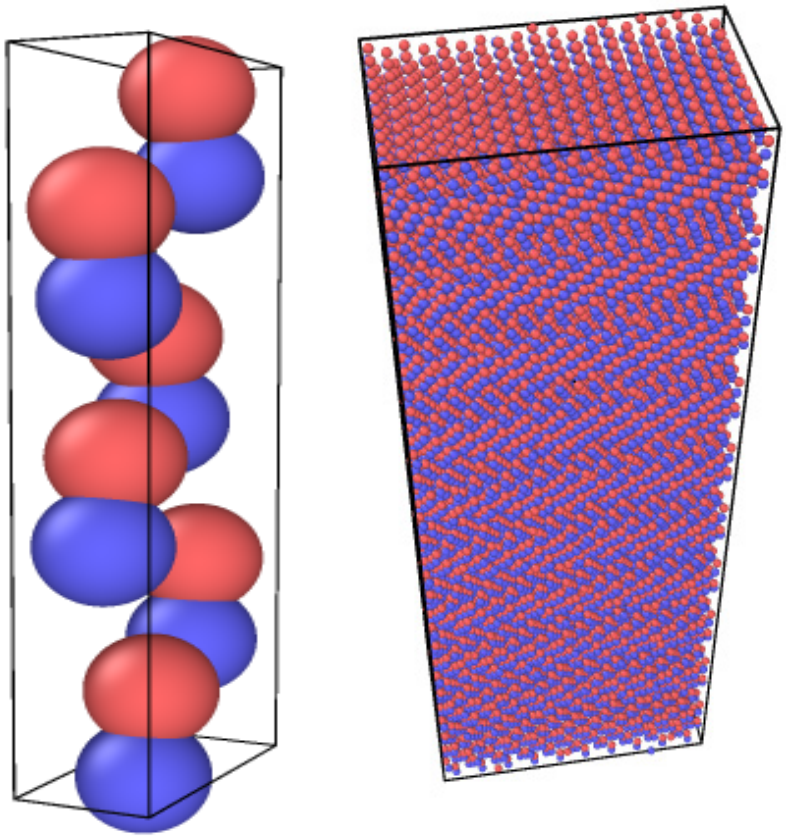

Figure 1.—6H SiC primitive cell (left) and a supercell (right) of size 10×10×10 (23,040 atoms).

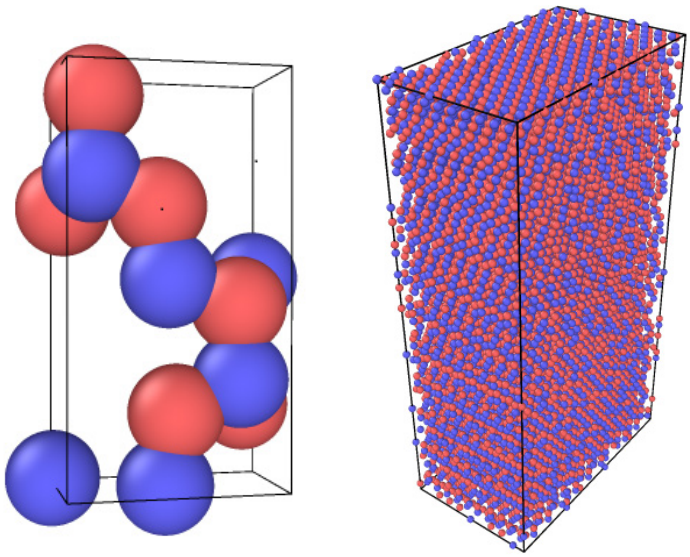

Figure 2.—4H SiC primitive cell (left) and a supercell (right) of size 10×10×10 (16,000 atoms).

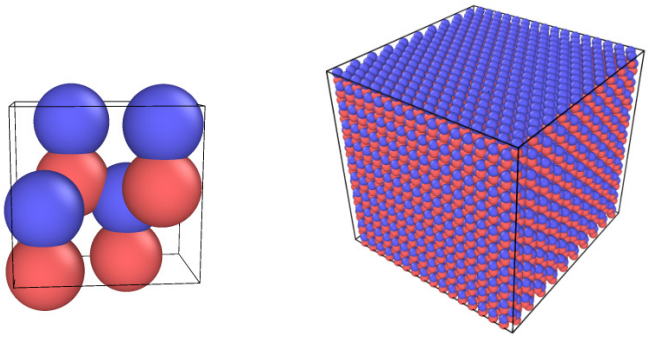

Figure 3.—Wurtzite SiC (2H) primitive cell (left) and a supercell (right) of size 17×10×10 (13,200 atoms).

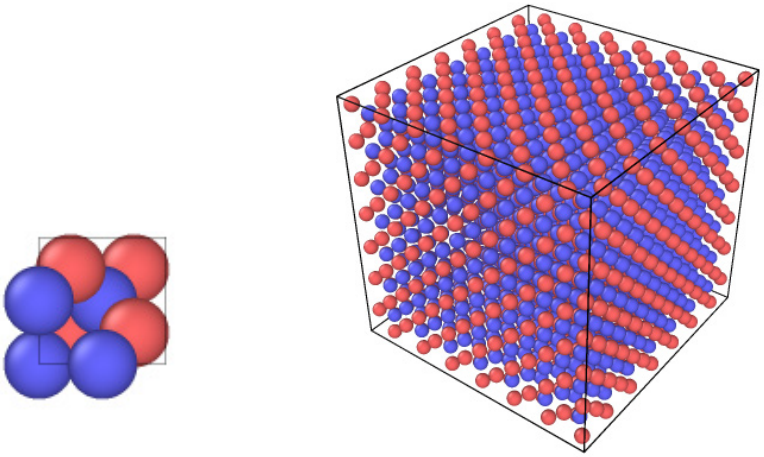

Figure 4.—β-SiC (3C) primitive cell (left) and a supercell (right) of size 15×15×15 (2,471 atoms).

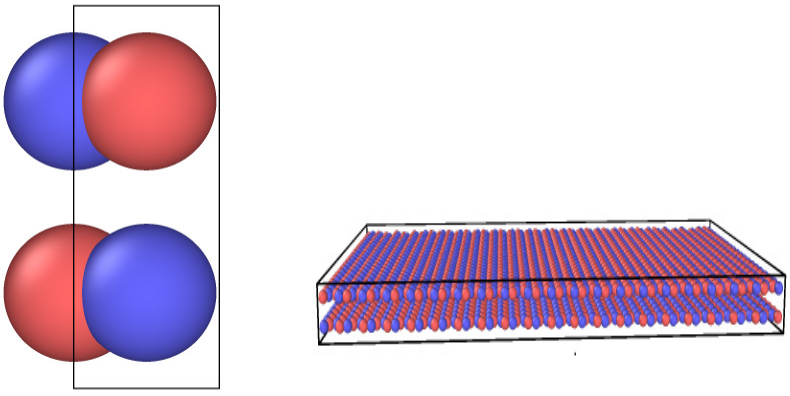

Figure 5.—Bilayer h-BN primitive cell (left) and a supercell (right) of size 20×20×1 (3,192 atoms).

$$a_1 = \frac{1}{2}ai - \frac{\sqrt{3}}{2}aj \tag{1a}$$

$$a_2 = \frac{1}{2}ai + \frac{\sqrt{3}}{2}aj \tag{1b}$$

$$a_3 = ck \tag{1c}$$

where, a = 3.08129Å and c/a = 4.90695780014 for 6H SiC and a = 3.08051Å and c/a = 3.27374363336 for 4H SiC. The primitive cells and supercells for 6H-SiC and 4H-SiC are shown in Figure 1 and Figure 2, respectively. Equation (1) also describes the primitive vector for the wurtzite 2H SiC structure. The primitive cell and an 11×7×7 supercell are shown in Figure 3. The 2H SiC structure is described with a = 3.072 Å and c = 5.041152 Å (Ref. 4).

The β-SiC (3C) was constructed with primitive vectors expressed as

$$a_1 = \frac{1}{2}aj - \frac{1}{2}ak \tag{2a}$$

$$a_2 = \frac{1}{2}ai + \frac{1}{2}ak \tag{2b}$$

$$a_3 = \frac{1}{2}ai + \frac{1}{2}aj \tag{2c}$$

where a = 4.3596 Å. The primitive cell and supercell for β-SiC (3C) structure are shown in Figure 4.

The structure for bilayer h-BN was modeled using the primitive vectors given by Reference 6

$$a_1 = \frac{\sqrt{3}}{2}ai - \frac{1}{2}aj \tag{3a}$$

$$a_2 = \frac{\sqrt{3}}{2}ai + \frac{1}{2}aj \tag{3b}$$

$$a_3 = ck \tag{3c}$$

where a = 2.50399 Å and c = 6.6612 Å. Both the unit cell and supercell are shown in Figure 5.

Then, MD simulations were performed using the NVT (constant number of atoms, volume, and temperature) ensemble at 300 K for 100 ps in order to relax the structures. Minimization was performed over 100 ps at a temperature of 300 K using the conjugate gradient stopping criterion to further reduce the internal forces and residual stresses that were created from the initial construction of the bonds and the bond angles. After the initial relaxation process was completed, the final equilibration of the system was done under the NPT ensemble at 300 K for 1000 ps using a time step of 0.08 fs and Nose-Hoover barostat and thermostat.

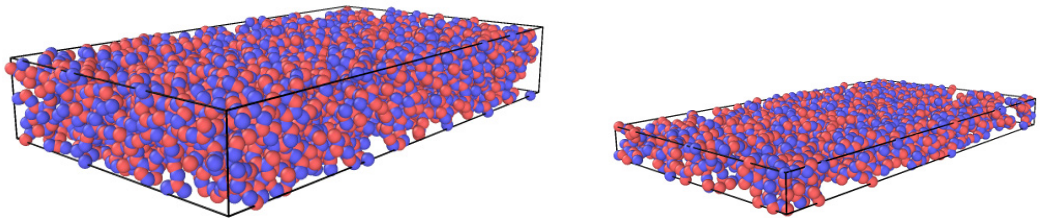

Figure 6.—a-BN structure from four (left) and two (right) layers of h-BN.

Modeling and Simulation of Amorphous Boron Nitride

The amorphous form of boron nitride (a-BN) is the dominant phase in most BN coatings (Refs. 8 and 9). The properties, and directionality of h-BN and a-BN are disparate. Thus, by changing the amount of h-BN within an a-BN matrix, it is possible to tailor its microstructural and mechanical properties to meet engineering needs. The development of computational material modeling to understand atomistic structure of a-BN, in conjunction with h-BN, has an important impact as this allows engineers not to only predict materials properties but also design materials for specific applications.

For this reason, a-BN models were prepared from crystalized h-BN models using a heating and cooling process. First, the h-BN was gradually heated in the NPT ensemble to a temperature of 6000 K. In reality, h-BN melting temperature is about 3,400 K (Ref. 27). In MD simulations, high temperature is used to reduce the computational time. Heating at high temperature for sufficient time melts the h-BN model by completely removing the memory of the initial crystalline configuration. Then the amorphous structure was simulated for 200 ps in the NPT ensemble before it was subjected to cooling to room temperature under the NVT ensemble at a quenching rate 100 K/ps. This nonequilibrium cooling establishes the formation of amorphous structure after solidification. The material system was finally equilibrated in NPT ensemble at 300 K for 200 ps before being evaluating its mechanical properties. In this study, two, four, five, and ten layers of h-BN were utilized for the development of amorphous structures in order to assess the influence of number of layers on predicted properties. As an example, the amorphous structure resulting from the heating and quenching of four and two h-BN layers, respectively, is shown in Figure 6. It is important to note that different cooling rates have been used in the literature ranging from 0.5 to 100 K/ps for different ceramic composites such as SiC and glass (Refs. 28 and 29). The upper limit (100 K/ps) was selected to model BN for high amorphous content in this study.

Modeling and Simulation of Crystalline Silicon

A crystalline Si model was constructed using the LAMMPS package with Reactive force field (ReaxFF) potentials from the primitive vectors expressed as:

$$a_1 = \frac{1}{2}aj - \frac{1}{2}ak \tag{4a}$$

$$a_2 = \frac{1}{2}ai + \frac{1}{2}ak \tag{4b}$$

$$a_3 = \frac{1}{2}ai + \frac{1}{2}aj \tag{4c}$$

where a = 5.43070 Å. ReaxFF was chosen *in lieu* of the Tersoff Potential for Si because it provides superior accuracy for Si, but at an added computational expense. The primitive cell and supercell for silicon utilized in this study are shown in Figure 7.

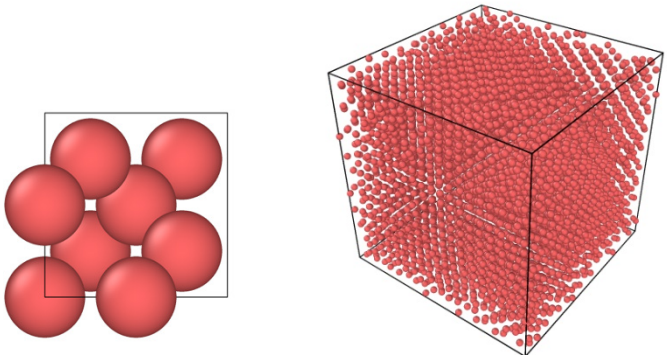

Figure 7.—The primitive cell (left) and supercell (right) of size 20×20×20 for silicon comprises 7,531 atoms.

ReaxFF was utilized for evaluating the properties of silicon because the Tersoff potential elastic property results showed a significant deviation from available experimental data. Then, MD simulations were performed using the NVT ensemble at 300 K for 100 ps in order to relax the structures. Minimization was performed at a temperature of 300 K using the conjugate gradient stopping criterion. After the initial relaxation process was completed, the final equilibration of the system was performed under the NPT ensemble at 300 K for 500 ps using a time step of 0.08 fs and Nose-Hoover barostat and thermostat.

Calculating Elastic Properties Using Molecular Dynamics

The equilibrated structure was mechanically deformed to obtain the required stress-strain relationship for evaluating the elastic constants. A distinct displacement vector was imposed to determine each elastic constant. For the case of elastic moduli, an axial strain is applied on the periodic models using the "fix deform" command in LAMMPS under the NPH (constant number of atoms, pressure, and enthalpy) ensemble at one atmosphere and a temperature of 300 K. This allows the Poisson's effect on two orthogonal directions to be calculated. The corresponding stress component in the axial direction was determined for a complete stress-strain response. NPH simulations were run for 1000 ps with time steps of 0.08 fs. The displacement was applied incrementally at every time step in such a way that the desired strain magnitude of 0.01 was attained at the end of 1000 ps. From each time step, the overall elastic modulus of the model (in the loading direction) was obtained from the plot of the stress-strain curve.

To obtain the stress-strain curve during the tensile loading, the virial stress $\sigma_{\alpha\beta}$ (Refs. 20 and 30) was computed from the equation

$$\sigma_{\alpha\beta} = \frac{1}{V}\left(\sum_{i=1}^{N} m v_{\alpha}^{i} v_{\beta}^{i} + \frac{1}{2}\sum_{i=1}^{N-1}\sum_{j=i+1}^{N} r_{ij,\alpha}^{N-1} F_{ij,\beta}\right) \tag{5}$$

where V is the total volume of the material system used in the simulation cell, α and β are the indices in the Cartesian coordinate system, m and v_{α}^{i} denote the mass and α-component velocity of the atom i, $r_{ij,\alpha}$ and $F_{ij,\beta}$ denote the α-component of the separation and the β-component of the force between atoms i and j, respectively. The cumulative magnitude of the applied strain was 0.01. A linear regression analysis was performed on the MD data to obtain the corresponding elastic modulus. The loading direction was varied in order to obtain the other elastic moduli. It should be noted that the above virial stress is the true stress. However, engineering stress, σ, was obtained using Equations (6) and (7).

$$\sigma = \frac{\sigma_{\alpha\beta}}{(1+\varepsilon)} \tag{6}$$

$$\varepsilon = \frac{L - L_o}{L_o} \tag{7}$$

where L and L_o are the instantaneous and original length in the loading direction, respectively and ε is the engineering strain.

It should be noted that the Poisson's effect on two orthogonal directions during uniaxial deformations for obtaining stresses was also evaluated using a linear regression analysis to obtain the in-plane Poisson's ratio. Its value for each model was determined from the plot of longitudinal strain versus lateral strain.

Also, a planar incremental shear strain was applied to each MD models, except Si. The corresponding shear stress τ_{xy} was computed for each time step. This simulation was performed using the NVT ensemble at 300 K and a pressure of one atmosphere at a constant engineering shear strain rate of 10^{-5}/ps. A linear regression analysis was used to obtain the simulated stress-strain from the data to obtain the shear modulus (G). However, the Si model was assumed to be isotropic, and this G was computed from the simulated elastic modulus E and Poisson's ratio ν using the expression G = E/2*(1+ ν).

Results and Discussions

The α-SiC structures, consisting of 6H SiC, 4H SiC, and 2H SiC, β-SiC (3C), h-BN, a-BN, and Si were created in LAMMPS. As stated before, the elastic moduli, shear moduli, and Poisson's ratios for each model were obtained from plots of stress-strain curves using regression analysis for each model evaluated in this study. Specifically, the raw data utilized to evaluate the longitudinal elastic modulus (E_x) for 6H SiC with small (23,040 atoms) and large (329,280 atoms) models are shown in Figure 8. Slight fluctuations in the stress-strain data were observed for the small model (the plot is wider and thicker) as a result of smaller size of the system. For the larger system, these fluctuations were less significant. However, the average value of E_x obtained from three different smaller models, 543.19 GPa as shown in Table 1, was comparable to the slope obtained from the larger model (E_x = 609.569 GPa).

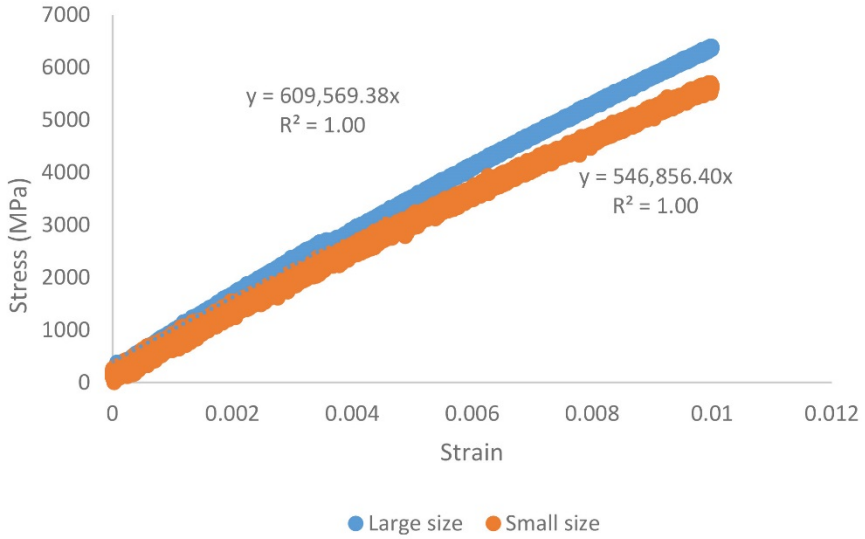

Figure 8.—Stress–strain curves for large and small 6H SiC sizes.

TABLE 1.—ELASTIC RESPONSE OF 6H SiC USING TERSOFF AT $\dot{\varepsilon} = 10^7$/s

Property	Sample 1	Sample 2	Sample 3	Average	Expt (Ref. 13)
E_x (GPa)	546.8560	537.768	544.946	543.19	473.417
E_y (GPa)	539.4410	536.8980	543.946	539.933	473.417
E_z (GPa)	612.0060	608.1430	633.749	617.966	544.188
G_{xy} (GPa)	252.7710	249.9730	254.459	252.401	195
G_{xz} (GPa)	225.9860	229.8690	221.512	225.789	163
G_{yz} (GPa)	219.4410	217.3560	219.582	218.793	163
ν_{xy}	0.23040	0.2188	0.2378	0.2290	0.2139
ν_{xz}	0.0840	0.0799	0.0797	0.0812	0.0739
ν_{yz}	0.0988	0.0941	0.0954	0.0961	0.0739

Despite the fact that all SiC polytypes chemically consist of 50 percent carbon atoms covalently bonded with 50 percent silicon atoms, these polytypes are characterized by their stacking sequence of biatom layers of the SiC structure. The 6H SiC is composed of two-third cubic and one-third hexagonal bonds. However, the overall symmetry is hexagonal for 6H SiC, despite the cubic bonds which are present. Since this is a hexagonal material, there are five independent elastic constants required to fully characterize its elastic properties (i.e., transversely isotropic material behavior). It can be seen in Table 1 that the elastic moduli were nearly the same in the planar directions (x and y) with a noticeable difference in the direction normal to the plane (z). Similar to ν_{xy} that is shown in Table 1, the Poisson's ratio $\nu_{yx} = 0.2094$ was evaluated from the MD model in order to verify the reciprocity relationships, and these relationships hold true. Other planes, xz and yz were also confirmed for consistency. Experimental results from the literature (Ref. 13) are also shown in Table 1. The MD predictions compare reasonably well with the experimental data. Furthermore, each of the three realizations (samples) had similar properties, indicating that the average predicted material properties were independent of minor randomizations.

The predicted mechanical properties of the other, α-SiC (4H SiC and 2H SiC) polytypes are shown in Table 2 and Table 3 along with available experimental data. The 4H SiC consists of an equal number of cubic and hexagonal bonds, but the overall symmetry is hexagonal. The 2H SiC (wurtzite) contains purely hexagonal bonds. The elastic moduli vary from one structure to the other as well as the degree of anisotropy. Additionally, the predicted shear moduli and Poisson's ratios are shown in Table 2 and Table 3. These simulated properties are also compared with experimental values. As with the 6H SiC, the properties of the 4H SiC and 2H SiC structures are over-predicted. The predictions of the planar properties of the wurzite SiC bound the results obtained from the literature using first principles and all predictions match reasonably well with the DFT data (Ref. 31). In general, no significant scatter was observed in both the 4H and 2H SiC predicted elastic constants. However, some scatter was noted in the predicted moduli for the 4H SiC. The predicted mechanical properties of β-SiC (3C) as revealed by MD simulation in comparison with other results in literature are shown in Table 4. The 3C SiC is the only form of SiC with an entirely cubic crystal lattice structure. The number "3" refers to the number of layers required for periodicity. From the data in Table 4, the 3C SiC was observed to be reasonably isotropic. The MD predictions also match closely with experimental data (Ref. 15) and DFT simulations (Ref. 5). Similar to the α-SiC structures, no significant scatter was observed in the elastic constants for the different samples.

As an aside, MD techniques can offer significant insight into the microstructural behavior of materials where experimental data is not available on one hand, and also provide confidence in available experimental data on the other. For example, Sola et al. (Ref. 32) performed nanoindentation of Sylramic SiC fibers (specific SiC structure unknown) and obtained an E_x of 315.74 ± 39.12, 322.74 ± 34.23, and 315.71 ± 16.38 for three distinct Sylramic fibers. Even though it was stated that the fibers consist other impurities such as TiB_2 (3 percent) and B_4C (1 percent), the results from Table 4 suggest that the 96 percent SiC in Sylramic fibers consists predominantly of β-SiC (3C).

TABLE 2.—ELASTIC RESPONSE OF 4H SiC USING TERSOFF AT $\dot{\varepsilon} = 10^7$/s

Property	Sample 1	Sample 2	Sample 3	Average	Expt (Ref. 13)
E_x (GPa)	626.6300	608.5100	590.4000	608.5120	476.1904
E_y (GPa)	623.2600	436.1500	529.7100	529.7060	476.1904
E_z (GPa)	671.4200	699.1400	587.3700	652.6440	526.3157
G_{xy} (GPa)	261.1130	261.8910	266.7370	263.2470	199.5000
G_{xz} (GPa)	224.7180	225.0370	226.5980	225.4510	159.0000
G_{yz} (GPa)	224.9650	226.4510	224.8920	225.4360	159.0000
ν_{xy}	0.2106	0.2115	0.2130	0.2117	0.1905
ν_{xz}	0.1037	0.1051	0.1056	0.1048	0.09524
ν_{yz}	0.0766	0.0787	0.0841	0.0798	0.09524

TABLE 3.—ELASTIC RESPONSE OF 2H SiC USING TERSOFF AT $\dot{\varepsilon} = 10^7$/s

Property	Sample 1	Sample 2	Sample 3	Average	DFT (Ref. 31)
E_x (GPa)	439.5820	440.1020	434.0880	437.9240	500.0000
E_y (GPa)	586.3300	585.5140	584.6770	585.5070	500.0000
E_z (GPa)	600.6640	604.8140	596.5140	600.6640	588.0000
G_{xy} (GPa)	146.6670	148.0210	148.1900	147.6260	162.0000
G_{xz} (GPa)	165.4130	166.3270	163.9500	165.2300	162.0000
G_{yz} (GPa)	226.0100	224.9270	225.5660	225.5010	212.0000
ν_{xy}	0.2011	0.2015	0.2013	0.2013	0.2000
ν_{xz}	0.0887	0.0895	0.0852	0.0878	0.1000
ν_{yz}	0.0755	0.0691	0.0789	0.0745	0.1000

TABLE 4.—ELASTIC RESPONSE OF β-SiC (3C) USING TERSOFF AT $\dot{\varepsilon} = 10^7$/s

Property	Sample 1	Sample 2	Sample 3	Average	Expt (Ref. 15)	DFT (Ref. 5)
E_x (GPa)	339.6860	336.5030	343.8110	340.0000	330±50	----------
E_y (GPa)	347.5010	314.3410	367.9980	343.2800	----------	347.4690
E_z (GPa)	343.2800	311.8040	321.1160	325.4000	----------	----------
G_{xy} (GPa)	194.8840	195.8780	196.4790	195.7470	----------	----------
G_{xz} (GPa)	202.445	203.9210	202.844	203. 070	----------	203.8760
G_{yz} (GPa)	181.668	180.895	183.404	181.9890	----------	----------
ν_{xy}	0.2544	0.2601	0.2529	0.2558	----------	0.2200
ν_{xz}	0.2396	0.2453	0.2477	0.2442	----------	----------
ν_{yz}	0.2532	0.2571	0.2535	0.2546	----------	----------

TABLE 5.—ELASTIC RESPONSE OF h-BN USING TERSOFF AT $\dot{\varepsilon} = 10^7$/s

Property	Sample 1	Sample 2	Sample 3	Average	MD (Ref. 20) $\dot{\varepsilon} = 10^7$/s	Expt (Ref. 12)
E_x (GPa)	691.4580	684.8000	710.3800	695.5460	739.9000	775.7831
E_y (GPa)	695.4580	688.7160	702.7160	695.6280	692.7000	775.7831
G_{xy} (GPa)	268.1120	266.4030	266.7850	267.1000	----------	7.70000
ν_{xy}	0.2895	0.2853	0.3237	0.2995	----------	0.20838

The predicted elastic properties of h-BN have also been compared with available experimental data (Ref. 12) and the MD computational results (Ref. 20). These are shown in Table 5. It can be seen from the elastic properties in Table 5 that the h-BN is transversely isotropic, and the in-plane elastic modulus (E) was greater than that for any of the other SiC microstructures. No significant scatter in the properties were observed for the three samples. The elastic properties for h-BN compares well with both MD and experimental data. However, there is a significant difference in the value of the in-plane shear modulus G between the MD result and experimental data. Giving that BN has planar isotropic behavior, it can be inferred that the value of G can be estimated from $E/2*(1+\nu)$. Such an estimate is closer to the MD result than the experiment result from Reference 12. The out-of-plane properties for the h-BN are not given because they are insignificant. This is due to the fact that the h-BN layers are only bonded together through van der Waals interactions.

TABLE 6.—ELASTIC RESPONSE OF a-BN USING TERSOFF AT $\dot{\varepsilon} = 10^7/s$

Property	2-layered	4-layered	5-layered	10-layered
E_x (GPa)	49.9780	43.4130	46.3940	50.3710
E_y (GPa)	52.3360	49.3270	46.7390	47.7820
E_z (GPa)	79.6740	51.4950	56.4200	49.0610
G_{xy} (GPa)	12.8590	17.3410	16.1680	20.0930
ν_{xy}	0.3242	0.3067	0.2892	0.3206
ν_{yx}	0.3290	0.3510	0.2974	0.3070

TABLE 7.—ELASTIC RESPONSE OF Si USING ReaxFF AT $\dot{\varepsilon} = 10^7/s$

Property	Sample 1	Sample 2	Sample 3	Average	Expt. (Ref. 33)
E_x (GPa)	144.5710	145.3160	145.236	145.0410	130.0000
E_y (GPa)	140.9820	142.0530	142.635	141.8900	130.0000
E_z (GPa)	143.4430	145.8270	141.779	143.6830	130.0000
G_{xy} (GPa)	54.7452	55.0147	54.9720	54.9106	79.6000
G_{xz} (GPa)	55.1461	55.4176	55.3997	55.3215	79.6000
G_{yz} (GPa)	53.6747	54.0660	54.2958	54.0125	79.6000
ν_{xy}	0.3204	0.3207	0.3210	0.3207	0.2800
ν_{xz}	0.3108	0.3111	0.3108	0.3109	0.2800
ν_{yz}	0.3133	0.3137	0.3135	0.3135	0.2800

The predicted a-BN mechanical properties are shown in Table 6. It can be seen that there is a tremendous reduction in both the elastic and shear moduli compared with those of the h-BN crystalline structure in Table 5. Interfacial BN coatings typically exhibit low stiffness values because they are composed predominantly of a-BN, with a very small fraction of h-BN (Refs. 8 and 9). However, the amount of h-BN can be controlled to tailor the properties of an interfacial coating. Furthermore, Table 6 shows that there is no agglomeration effect, i.e., effect of number of layer or clumping, on the mechanical properties of amorphous boron nitride. A slight difference in the elastic moduli was observed. However, this difference decreases (as expected) when the simulation volume increases. It is important to note that only one simulation was performed for each a-BN sample since the predicted material properties of the models in the present MD simulations were independent of minor randomizations.

Finally, the predicted elastic properties of crystalline Si are given in Table 7. The properties in the different directions are consistent with the isotropic nature of crystalline Si as seen in Table 7 and did not significantly vary among the three samples. As stated in Reference 33, the possible values for the elastic modulus range from 130 to 188 GPa, and those for Poisson's ratio range from 0.048 to 0.400.

Conclusion

MD was used to predict the mechanical properties of the various constituent materials that compose SiC/SiC composites. This represents foundational work towards developing a multiscale modeling framework, wherein the atomic microstructure is coupled to the composite material performance, for SiC/SiC composites. The microstructures of the constituents in the SiC/SiC composite contain a variety of different phases. Crystalline α-(6H, 4H, and 2H) and β-SiC (3C), crystalline (layered) and amorphous BN, and silicon (Si) models were constructed in LAMMPS using Tersoff potential force field, while the Reactive force field was used for Si. These structures were equilibrated to remove residual stress before they were evaluated for their mechanical properties. A total of 115 MD simulations were performed to arrive at the data reported herein. In many cases the MD predictions matched well with previously available experimental or other simulation data. It is expected that larger size and number of simulations would further improve the predicted results. The work could also be extended to infer the phase contents of the various constituents in SiC/SiC composites. Moreover, the phase content could be adjusted, through microstructural modeling, to optimize performance of the composite.

References

1. Bhatt R.T., Chen Y.L., Morscher G.N., Microstructure and Tensile Properties of BN/SiC Coated Hi-nicalon, and Sylramic SiC Fiber Preforms. NASA/TM—2001-210695.
2. Katoh Y., Snead L.L., Henager Jr. C.H., Nozawa T., Hinoki T., Ivekovíc, Novak S., Gpnzalez de Vicente S.M. Current Status and Recent Research Achievements in SiC/SiC Composites. Journal of Nuclear Materials 2014; 455:397-397.
3. Meyer P., Waas A.M. FEM Predictions of Damage in Continuous Fiber Ceramic Matrix Composites under Transverse Tension Using the Crack Band Method. Acta Materialia 2016; 102: 292-303.
4. Park C.H., Cheong B., Lee K., Chang K.J., Structural and Electronic Properties of Cubic, 2H, 4H, and 6HSiC.. Physical Review B 1994; 49 (7): 4485-4493.
5. Bauer A., Reischauer P., Krausslich J., Schell N., Matz W., Goetz K. Structure Refinement of Silicon Carbide Polytypes 4H and 6H: Unambiguous Determination of the Refinement Parameters, Acta Crystallogr. Sec. A 2001*;* 57: 60-67, doi:10.1107/S0108767300012915.
6. Liu X., Li L., Lu F., Optical Properties and Mechanical Properties of C, Si, Ge and 3C-SiC Materials Calculated From First Principles Teory. Central Eueopean Journal of Physics 2008; Author version, 1-13.
7. Vashishta P., Kalia R.K., Nakano A., Interaction Potential for Silicon Carbide: A Molecular Dynamics Study of Elastic Constants and Vibrational Density of States for Crystalline and Amorphous Silicon Carbide. Journal of Applied Physics 2007; 101 (103515): 1-12.
8. Singh R.N., Brun M.K., Effect of Boron Nitride Coating on Fiber-Matrix Interactions. Ceram. Eng. Sci. Proc. (1987); 8[7-8]: 636-643.
9. Morscher G.M., Yun H.M., DiCarlo J.A., Thomas-Ogbuji L., Effect of a Boron Nitride Interphase that Debonds Between the Interphase and the Matrix in SiC/SiC Composites. Journal of the American Ceramic Society 2008; 87 (1): 104-112
10. Ortona A., Donato A., Filacchioni G., De Angelis, U., La Barbera, A., Nannetti C., Riccardi B., Yeatman J., SiC–SiC CMC Manufacturing by Hybrid CVI–PIP Techniques: Process Optimisation. Fusion Engineering and Design 2000; 51:159-163. 10.1016/S0920-3796(00)00310-0.
11. Hillig W.B., Melt Infiltration Approach to Ceramic Matrix Composites. Journal of the American Ceramic Society 1988; 71[2]: c96-c99.
12. Bosak A., Serrano J., Krisch M., Watanabe K., Taniguchi T., Kanda H., Elasticity of Hexagonal Boron Nitride Inelastic X-ray Scattering Measurements. Physical Review B 2006*;* 73 (4) id.041402.
13. Kamitani K., Grimsditch M., Nipko J.C., Loong C.K., Okada M., Kimura I., The Elastic Constant of Silica Carbide: A Brillouin-Scattering Study of 4H and 6H SiC Single crystal. Journal of Applied Physics 1997; 82 (6): 3152-3154.
14. Harris G.L., Young's Modulus of SiC*,* in Properties of Silicon Carbide. Ed. Harris, G.L., EMIS Datareviews Series, N13, 1995c, 8.
15. Pozzi, M., Hassan M., Harris A.J., Burdess J.S., Jiang L., Lee K.K., Cheung R., Phelps J.S., Mechanical Properties of a 3C-SiC Film between Room Temperature and 600°C. Journal of Physics D: Applied Physics 2007; 40 (11).
16. Zhi C., Bando Y., Tang C., Kuwahara H., Golberg D., Large-scale Fabrication of Boron Nitride Nanosheets and Their Utilization in Polymeric Composites with Improved Thermal and Mechanical Properties. Advanced Materials 2009; 21 (28): 2889-2893.
17. Jackson K.M., Dirras G.F., Edwards R.L., Sharpe WN. Mechanical Properties of 3C Thin-film Silicon Carbide. Symposium B-Materials Science of Microelectromechanical Systems (MEMS) Devices IV), 687. https://doi.org/10.1557/PROC-687-B6.3.
18. Li L., Sola F., Xia Z.H., Yang Y.Q., Effect of Amorphous Carbon Coatings on the Mechanical Behavior of Silicon Carbide Nanowire. Journal of Applied Physics 2012; 111, 094306: doi: http://dx.doi.org/10.1063/1.4711090.

19. Crocombette J., Dumazer C., Hoang N.Q., Molecular dynamics Modeling of the Thermal Conductivity of Irradiated SiC as a Function of Cascade Overlap. Journal of Applied Physics 2007; 101, 023527: doi. http://dx,doi.org/10.1063/1.2431397.
20. Zhao S., Xue J., Mechanical Properties of Hybrid Graphene and Hexagonal Boron Nitride Sheets as Revealed by Molecular Dynamic Simulations. Journal of Physics D: Applied Physics 2013; 46, doi:10.1088/0022.3727/46/13/135303.
21. Natsuki T., Natsuki J., The Prediction of Mechanical Properties for Hexagonal Boron Nitride Nanosheets Using Molecular Mechanics Model. J. Applied Physics A. 2017; 123:283, https://doi.org/10.1007/s0033.
22. Boldrin L., Scarpa F., Chowdhury R., Adhikari S., Effective Mechanical Properties of Hexagonal Boron Nitride Nanosheets. Nanotechnology 2011; 22 (50), URL: https://doi.org/10.1088/0957-4484/22/50/505702.
23. Mirnezhad M., Ansari R., Rouhi H., Mechanical Properties of Multilayer Boron Nitride with Different Stacking Orders. Superlattices and Microstructures 2013; 53: 223-231. https://doi.org/10.1016/j.spmi.2012.10.016.
24. Peng Q., Ji W. De S., Mechanical Properties of the Hexagonal Boron Nitride Monolayer: *Ab initio* Study. Computational Materials Science 2012; 56: 11-17.
25. Ooi N., Rairkar A., Lindsley L. Adams JB., Electronic Structure and Bonding in Hexagonal Boron Nitride. Journal of Physics: Condensed Matter 2006; 18: 97-115.
26. Ooi N., Rajan V., Gottlieb J., Cathering Y., Adams JB., Structural Properties of Hexagonal Boron Nitride. Modelling and Simulation in Materials Science and Engineering 2006; 14 (3): 515-535.
27. Solozhenko V.L., Turkevich V.Z., Refined Diagram of Boron Nitride. Journal of Phys. Chem. 1999; 103 (15): 2903-2905.
28. Xue K., Niu L., Shi H. Effect of Quench Rates on the Short- and Medium-range Orders of Amorphous Silicon Carbide: A Molecular-Dynamics Study. Journal of Applied Physics 2008; 104: 1-7.
29. Chowdhury S.C., Haque B.Z., Gillespie J.W., Molecular Dynamic Simulations of the Structure and Mechanical Properties of Silica Glass Using ReaxFF. Journal of Material Science 2016; 51: 10139-10159.
30. Subramaniyan A.K., Sun C.T., Continuum Interpretation of Virial Stress in Molecular Simulations. International Journal of Solids and Structures 2008; 45:4340-4346.
31. Sarasamak K., Limpijumnong S., Lambrecht WRL., Pressure-Dependent Elastic Constants and Sound Velocities of Wurtzite SiC, GaN, InN, ZnO, and CdSe, and their Relation to the High-Pressure Phase Transition: A First-Principles Study. Phys. Rev. B 2010; 82, 035201.
32. Sola F., Bhatt R., Mapping the Local Modulus of Sylramic Silicon Carbide Fibers by Nanoindentation. Materials Letters 2015; 159: 395-398.
33. Hopcroft M.A., Nis W.D., Kenny T.W., What is the Young's Modulus of Silicon? Journal of microelectromechanical Systems 2010; 19 (2): 229-238.